Biofunctionalized Ceramic with Self-Assembled Networks of Nanochannels

Hae Lin Jang,[†] Keunho Lee,[†] Chan Soon Kang,[†] Hye Kyoung Lee,[†] Hyo-Yong Ahn,[†] Hui-Yun Jeong,[†] Sunghak Park,[†] Seul Cham Kim,[†] Kyoungsuk Jin,[†] Jimin Park,[†] Tae-Youl Yang,[†] Jin Hong Kim,[†] Seon Ae Shin,[†] Heung Nam Han,[†] Kyu Hwan Oh,[†] Ho-Young Lee,[‡] Jun Lim,[§] Kug Sun Hong,[†] Malcolm L. Snead,*[,⊥] Jimmy Xu,*[,∥] and Ki Tae Nam*[,†]

[†]Department of Materials Science and Engineering, Seoul National University, Seoul, 151-744, Korea, [‡]Department of Nuclear Medicine, Seoul National University, Bundang Hospital, Seoul, 463-707, Korea, [§]Pohang Accelerator Laboratory, POSTECH, Pohang, 790-784, Korea, [⊥]Center for Craniofacial Molecular Biology, Herman Ostrow School of Dentistry, University of Southern California, Los Angeles, California 90033, United States, and [∥]School of Engineering and Department of Physics, Brown University, Providence, Rhode Island 02912, United States

ABSTRACT Nature designs circulatory systems with hierarchically organized networks of gradually tapered channels ranging from micrometer to nanometer in diameter. In most hard tissues in biological systems, fluid, gases, nutrients and wastes are constantly exchanged through such networks. Here, we developed a biologically inspired, hierarchically organized structure in ceramic to achieve effective permeation with minimum void region, using fabrication methods that create a long-range, highly interconnected nanochannel system in a ceramic biomaterial. This design of a synthetic model-material was implemented through a novel pressurized sintering process formulated to induce a gradual tapering in channel diameter based on pressure-dependent polymer agglomeration. The resulting system allows long-range, efficient transport of fluid and nutrients into sites and interfaces that conventional fluid conduction cannot reach without external force. We demonstrate the ability of mammalian bone-forming cells placed at the distal transport termination of the nanochannel system to proliferate in a manner dependent solely upon the supply of media by the self-powering nanochannels. This approach mimics the significant contribution that nanochannel transport plays in maintaining living hard tissues by providing nutrient supply that facilitates cell growth and differentiation, and thereby makes the ceramic composite "alive".

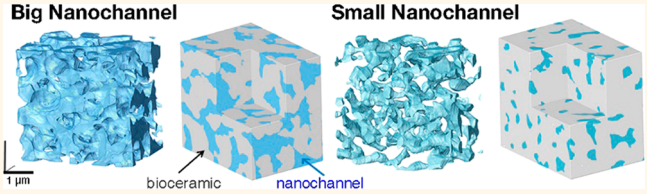

KEYWORDS: nanochannels · hierarchical structures · bioinspired · fluid transports · ceramics · pressure gradient sintering · polymer agglomeration

In nature, constructal law suggests that hierarchically arranged channels efficiently transport fluids and nutrients needed to enable and support biological activities.[1] For example, geometries of rivers, trees, and lungs generally evolve over time to enhance easier access of flow. In addition, gradual changes of surface tension are often built into the structures of natural systems, facilitating the collection of water on spider web silk, the transport of prey through the beaks of shorebirds and the desert beetle using its bumpy back to drink water.[2−4] In these systems, spontaneous fluid motion can be derived by differing surface roughness or narrowing channel geometry. Plant xylem and vascular capillaries are among the most well-known designs that combine these two principles. Such interconnected channels exist not only within soft tissues, but also within rigid hard tissues, such as bone, egg shell, crustacean tergite and nail.[5−9] Hierarchical circulation in bone was successfully demonstrated through inserting ink and analyzing its flow by microradiography and histology. Also, high resolution image techniques, such as field emission scanning electron microscopy (FESEM) and low voltage scanning electron microscopy (STEM) were utilized to show hierarchical channel structure in egg shell, tergite cuticle, and human nail, ranging from micrometer to nanometer. Gases and fluids are exchanged through channels linking the proximal and distal parts of these hard tissues to maintain pressure and/or to supply nutrients.

Recreating these natural nanoscale transport mechanisms in ceramic materials has remained a challenge. One constraint lies in the conflict between mechanical strength and permeation of microscale porous materials.[10] Another difficulty is in

* Address correspondence to mlsnead@usc.edu, jimmy_xu@brown.edu, nkitae@snu.ac.kr.

Received for review February 13, 2015 and accepted March 31, 2015.

Published online March 31, 2015
10.1021/acsnano.5b01052

the making of networked channels varying in diameter from micrometers to nanometers. Despite the difficulty in fabrication, numerous efforts have been made in synthetic systems to investigate the use of millimeter or microsized channels for controlling and facilitating fluidic conduction.[11−13] Here, we implemented a biomimetic transport system of interconnected networks of capillary channels ranging from micro- to nanoscale in diameters in a model ceramic biomaterial made of hydroxyapatite (HAP: $Ca_{10}(PO_4)_6(OH)_2$). The mechanisms for the fluidic supply in this material can be explained by the Laplace pressure model, which predicts a negative pressure gradient to arise from a nanochannel with a gradual narrowing diameter and thereby drive fluid flow toward the narrow end. In a channel with a gradually changing diameter, fluid transport is enhanced as the flow rate of fluid becomes greater than in a tube with a constant diameter. A similar kinetic advantage for fluid flow in hierarchically tapered channel structure was confirmed in prior experimental and theoretical works.[3,14−21] To build a network of gradually narrowing nanochannels into the ceramic biomaterial, we devised a novel pressurized sintering method, as detailed below.

RESULTS AND DISCUSSION

In order to obtain networked nanochannels, we utilized polymer agglomeration phenomena that naturally occur in the composite during sintering and are pressure-dependent. While previous reports on observation of polymer agglomeration were mostly in polymers based systems,[22,23] ours was in a ceramic-dominant system and achieved the desired formation of small (micro- to nanoscale) capillary channels due to polymer segregation. We chose to work with HAP and polyethylene glycol (PEG, $H(OCH_2CH_2)_nOH$), because of their biocompatibility and natural tendency of segregation. For a direct observation of the agglomeration tendency of PEG from HAP, we looked at the initial stage of PEG agglomeration from HAP below the PEG degradation temperature where PEG remained in the liquid state and HAP grains did not grow. To directly visualize these early polymer-segregation events, we made thin layers of PEG-HAP homogeneous mixture (PEG:HAP = 1:10) between two glass slides and used reflected, polarized light (Polarized Optical Microscopy, Olympus BX51) to distinguish PEG from HAP. After systematically applying heat and pressure on the PEG-HAP mixture, the observed images provided us a means of visualizing the polymer-agglomeration phenomena and supported the hypothesis of polymer agglomeration being an enabling mechanism for the formation of the pressure-dependent, dimension tunable, nanochannel networks. These observations take advantage of the fact that PEG converts into an ordered crystalline state after a melting−solidification process that is readily identified by its unique birefringence color pattern under polarized light. PEG agglomeration is shown *in situ* in Figure 1a,b, subjected

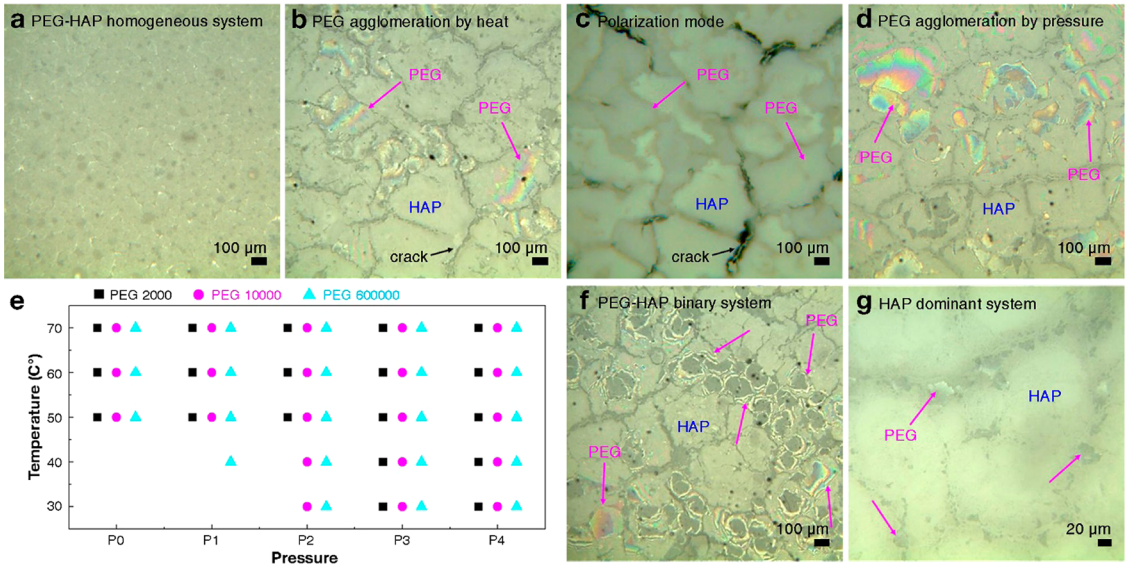

Figure 1. Polymer agglomeration between PEG and HAP is dependent on thermal energy and pressure. (a) Homogeneously mixed state of polyethylene glycol (PEG) and hydroxyapatite (HAP) in 1 to 10 ratio at room temperature and atmospheric pressure, observed by polarized optical microscopy. (b) Sample shown in "a" after heating at 70 °C for 2 h where agglomerated PEG crystallized and was observed by their unique color pattern in polarized light. The polarizing filters were parallel to each other. (c) The color pattern of PEG material appeared dark when the polarization of the reflected light from the crystallized PEG was parallel to either of the two perpendicular polarizers. (d) When pressure from the 0.8 kg mass of metal cubes was exerted on the HAP-PEG mixture without heating (*e.g.*, sample temperature of 30 °C) for 2 h, a similar PEG agglomerated pattern was observed. (e) Polymer agglomeration chart of PEG and HAP mixture (PEG:HAP = 1:10) as a function of temperature and pressure (maintained for 2 h). "*P*" represents the pressure exerted by 0.2 kg metal cube on the PEG-HAP mixture over an area of 3 cm × 3 cm, "2*P*" the pressure exerted by 0.4 kg and *etc.* (f) Agglomerated PEG in a PEG-HAP binary system (PEG:HAP = 1:1), after heating at 70 °C for 2 h. (g) Network of agglomerated PEG in a HAP ceramic dominant system (PEG:HAP = 1:100), after heating at 70 °C for 2 h.

to heating of a homogeneously mixed PEG-HAP composite. Separated PEG crystalline regions were revealed as a birefringence colored pattern when observed in reflected polarized light and these became darker when the polarization of the reflected light from the PEG was parallel to either direction of the perpendicular polarizers (Figure 1b-c). Notably, similar polymer agglomeration phenomenon occurred (Figure 1d) when we applied pressure to the PEG-HAP mixture at lower temperatures. In the absent of pressure, agglomeration of PEG started at higher temperatures. As the pressure increases, less thermal energy was required to induce agglomeration of PEG. From the findings shown in Figure 1e, we constructed a polymer agglomeration chart between HAP and various molecular weights of PEG, as a function of the temperature and the pressure. In addition, while polymer agglomeration was generally observed over a wide range of PEG to HAP ratios (Figure 1f,g), segregated PEG remained connected with each other, forming a network between HAP particles, especially prominently in the HAP dominant composite (PEG:HAP = 1:100). The network of agglomerated PEG forms the incipient channel for the interconnected capillary network observed after sintering. During the sintering process, PEG microchannels change into nanochannels due to the grain growth and densification of the HAP ceramic pellet.

We applied the knowledge visualized in the model experiments described above to engineer a network of dimension tunable nanochannels into three-dimensional ceramic composites. In order to generate gradient and networked capillaries, we devised a new sintering process that incorporated a polymer of selected molecular weight blended with HAP particles and subsequently sintered them under the influence of a unidirectional pressure gradient. Without the PEG and the pressure gradient, it is known and confirmed in our work too that HAP powders do not form interconnected nanochannels by conventional sintering at the same high temperature (1100 °C).[24−26] However, with the addition of PEG and an externally applied pressure gradient, a pressure-regulated process takes place during sintering that generated networked, interconnected pore structures, which eventually formed networked channels with a directionally tapered channel geometry. Interestingly, with sufficient PEG added for appreciable polymer aggregation, the size of the channel was proportional, instead of inversely proportional, to the amount of local pressure. As such, channels with gradually changing diameter could be controllably made by applying a pressure gradient during the sintering process.

The process we developed is one sharing the mechanisms revealed in several examples of phase-transitions that the polymer and ceramic composite could undergo with sufficient intake of energy such as heat or electricity.[27−29] In the present case, it is the combined mechanical and thermal energy that resulted in the formation of nanochannels and their networks through the polymer-segregation between PEG and HAP during the sintering of the hybrid composite (Figure S1, Supporting Information). The size of the pore generated during the sintering depends not only on the local pressure but also on the amount of PEG. The particularly strong dependence on the amount and the molecular weight of PEG are telling indicators of the agglomeration behavior of PEG being a key factor in the generation of pores. During our sintering process, the thermal energy and additional pressure allowed the PEG to detach from the HAP, diffuse, and aggregate.[30−33] After sintering reaches a peak temperature of 1100 °C, the PEG aggregates were completely burned out, leaving behind interconnected pores that form networked, tapered channels, which increase in size from one end to the other, perhaps counterintuitively, along the same direction of the applied pressure gradient.

In prior work performed in this field, pressurization during sintering was used as an aid to densify ceramic and a low concentration of polymer (*e.g.*, 0.01% by weight) was added as a binder.[34−36] However, our results suggested that increasing both the amount and the molecular weight of the polymer to about 10% by weight and 10 000 g mol^{-1} or more, respectively, would change the role of the polymer into a major determinant of the sintered ceramic structure. This finding, along with that of the counterintuitive dependence on pressure, was confirmed in all subsequent tests. Both parameters were utilized to make our ceramic sample, with its built-in networks of tapered channels with continuously narrowing diameter, from micrometer to nanometer, which are shown in fluid transport, biological cell viability and differentiation tests, to provide nutrient supply for cell growth and biomineralization activity.

For actual implementation of this particular pressurized-sintering concept, we created a pressure gradient by placing a triangular prism (wedge) made of metal directly on the PEG-HAP sample (Figure 2a). We labeled the pressure level along the long-axis of a PEG-HAP pellet, during sintering, from 0 to 12, corresponding to the pressure gradient exerted on the pellet. The greatest local pressure we applied to the PEG-HAP sample was 34.47 KPa (see Supporting Information, Note S1), achieved near the heavier end of the metal wedge with the loading gradually decreasing along the length of the wedge. More sophisticated mechanical stress controls could be deployed, some of which were tried, but the simpler method described here turned out to be also the better one to quantify the local pressure and its pressure gradient.

N_2 adsorption−desorption isotherm testing showed a gradual increase of internal porosity from one end to

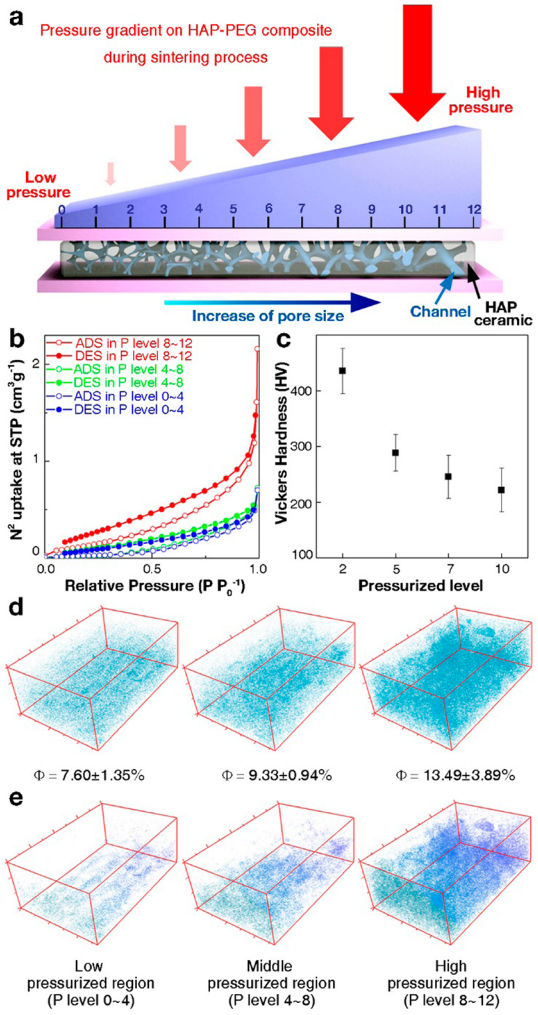

Figure 2. Generation of hierarchically networked and graded nanochannel structures in ceramic material through the application of unidirectional gradient of pressure during sintering. (a) A simple design for creating gradient pressure during sintering process and schematic representation of nanochannel with gradually changing diameter formed in HAP ceramic (NC-HAP) showing different porosity sections that correspond to different regions in the pressure gradient. Pressure levels (*P* level) were labeled from 0 to 12, corresponding to the pressure gradient exerted on an NC-HAP during sintering. As the pressure level increases during sintering process, the diameter of the channel (blue) in HAP ceramic (white) increases. (b) N_2 adsorption−desorption isotherm confirmed augmentation of porosity generated by the applied pressure. Amounts of N^2 ($cm^3\ g^{-1}$) adsorption (ADS) and desorption (DES), at standard temperature and pressure (STD), from the low (pressure level 0−4), middle (pressure level 4−8) and high (pressure level 8−12) pressure regions in NC-HAP are compared by relative pressure ($P\,P_0^{-1}$). (c) Micro-Vickers hardness was tested from each selected region of the NC-HAP. (d) Distribution of low-density pixels (blue) in the low (pressure level 0−4), middle (pressure level 4−8) and high (pressure level 8−12) pressure regions in NC-HAP during sintering obtained from X-ray micro-CT analysis, where their porosities (Φ) were measured by Archimedes' principle to be 7.60 ± 1.35%, 9.33 ± 0.94% and 13.49 ± 3.89%, respectively. (e) Selected image of fully connected low-density pixels with exterior regions, as revealed by the X-ray micro-CT data.

the other for the pressure-gradient generated HAP pellets, with the end that experienced the highest pressure becoming more porous (Figure 2b). The total pore volume increased from 0.001 $cm^3\ g^{-1}$ in the region of lowest pressure (pressure level 0−4) to 0.003 $cm^3\ g^{-1}$ in the region of highest pressure (pressure level 8−12), while the surface area also increased from 0.067 to 0.555 $m^2\ g^{-1}$. In addition, perhaps as expected, there was a gradual change of hardness from the end of the sample with greatest porosity to the other end (Figure 2c), further confirming the continuously changing gradient of porosity. In order to distinguish PEG-HAP samples generated in this way from nonporous or randomly porous HAP blocks, we refer to the resultant interior structure as nanochannel with gradually changing diameter formed in HAP ceramic (NC-HAP). The porosities of the low (pressure level 0−4), middle (pressure level 4−8) and high (pressure level 8−12) pressure sections of the NC-HAP during sintering were measured to be 7.60 ± 1.35%, 9.33 ± 0.94% and 13.49 ± 3.89% based upon Archimedes' principle ($n = 3$). By utilizing a micro-CT (ZEISS Xradia 510 Versa) with a resolution of 0.67 μm per pixel, we showed that pixels below the lower contrast threshold (corresponding to the low areal density characteristic of the material and thus the existence of many nanochannels inside the pixel region) were distributed throughout the NC-HAP sample (Figure 2d), while most of these low-density pixels were interconnected with the exterior (Figure 2e). This method based on setting the threshold in micro-CT based imaging is based on experimentally determined data and was adopted from published literature.[37] The interconnectivity of these low-density pixels was 21.5, 43.2 and 79.4% for the low (pressure level 0−4), middle (pressure level 4−8) and high (pressure level 8−12) pressure region of the NC-HAP, respectively. Such small diameter channels and their interconnectivity are supported by the PEG agglomeration observed by polarized light inspection of the initial sintering process, as shown in Figure 1.

The gradual change in pore size and their connection into networked channels was directly confirmed by three-dimensional reconstruction using SEM tomography of focused ion beam (FIB) dissected samples. For this analysis, as shown in the Figure 2a, we first divided an NC-HAP pellet into four segments corresponding to regions of the pressure gradient during sintering (pressure level 0−3, pressure level 3−6, pressure level 6−9 and pressure level 9−12), and subjected each segment to FIB milling into 15 nm increments with imaging by field-emission SEM (FESEM). Before conducting FIB-FESEM tomography, FESEM observation for each segment clearly showed that the formation of a porous structure was reinforced according to the pressure increment level from one end to the other end of the NC-HAP pellet (Figure S2). From the porosity analysis utilizing image analysis software ImageJ, the number of pores in all size ranges increased in

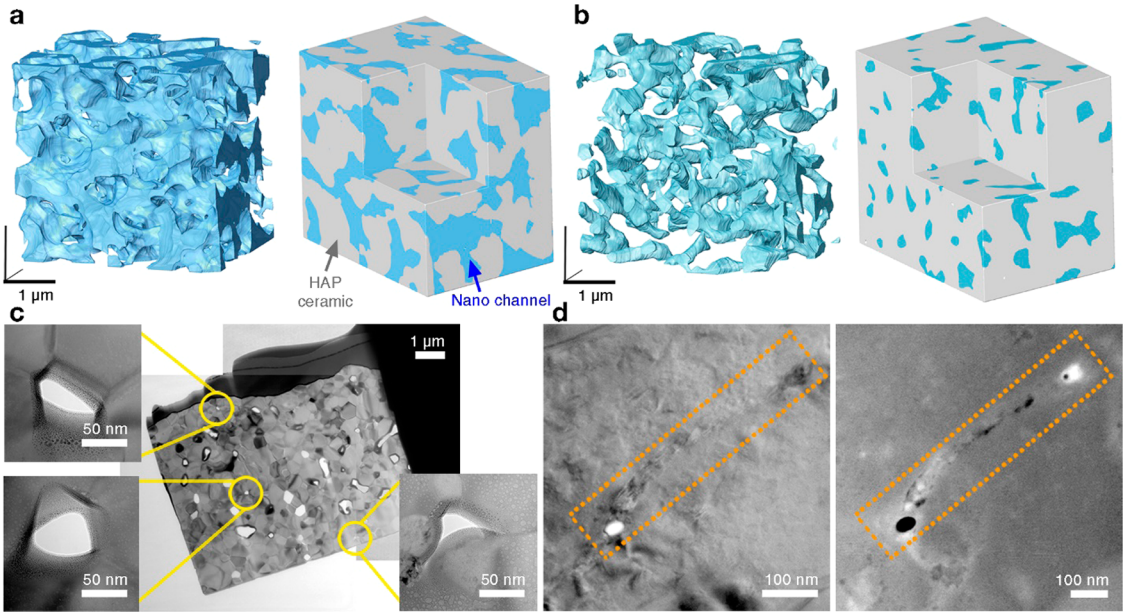

Figure 3. Electron microscopic characterization of nanochannel with gradually changing diameter formed in HAP ceramic (NC-HAP). (a) Three-dimensionally connected pore structures (blue) and HAP scaffold (gray) from the section with pressure level 6−9 were reconstructed by focused ion beam-field emission scanning electron microscopy (FIB-FESEM) tomography. (b) Three-dimensionally connected pore structure (blue) and scaffold (gray) from the section with pressure level 3−6 were reconstructed by FIB-FESEM tomography. (c) High resolution transmission electron microscopy (HRTEM) images of pores, visualized as cross sections of nanochannels from the section with pressure level 3−6. (d) HRTEM images from the section with pressure level 0−3. Nanochannel had approximately 20 nm width in both BF mode and STEM mode analysis.

the high-pressure region compared to those observed in the low-pressure region. This experimental strategy confirmed that the section with pressure level 9−12 had mostly pores of diameter larger than the micrometer scale (Figure S2). From the same NC-HAP sample, two other representative areas of the pellet that experienced different amounts of pressure (pressure level 6−9 and pressure level 3−6) were imaged along the pressure gradient at 15 nm intervals with 3D reconstruction of the inner structure created using the Amira imaging software. As shown in the 3D reconstructed images (Figure 3a,b) and videos (Movie S1), regions corresponding to pressure level 6−9, and pressure level 3−6, both manifest nanopores connected by channels. Furthermore, because of the pressure gradient used during sintering, we observed decreased porosity and channel diameter in the NC-HAP sample from pressure level 6−9 *versus* pressure level 3−6. Additionally, in the Movie S1, pore connectivity was identified when the NC-HAP sample was scanned along its axis. Pore connectivity was corroborated by 3D reconstruction of synchrotron X-ray imaging at the nanoscale as shown in the Movie S2.

For a direct visualization of nanochannels beyond the resolution limit of micro-CT and SEM, HRTEM analysis was performed for the segments of the NC-HAP sample corresponding to pressure level 3−6 and pressure level 0−3, as shown in Figure 3c,d. TEM samples were prepared with FIB and placed on a 3-post Cu grid. The width of pores, visualized by the contrast, was between 70 to 400 nm (Figure 3c and Figures S3 and S4). The number of pores in a given area (*ca.* 7.84 × 3.04 μm^2) was in the range of 40−50. It was also apparent that the shape of the pores is affected by the grain size of the HAP, which was roughly 300 to 1000 nm and is consistent with grain growth during the sintering process from the initial 80 nm particles to this relatively larger grain size. As shown in Figure 3d, very narrow channels, as small as 20 nm in width, also exist and these can be clearly seen in images from the segment with pressure gradient level 0−3.

To confirm that the pressurized-gradient sintering method can be generally applied to generate graded nanochannel (NC) structure in other inorganic material, we also tested the same methodology with whitlockite (WH: $Ca_{18}Mg_2(HPO_4)_2(PO_4)_{12}$) nanoparticles. Whitlockite is the second most abundant biomineral in human hard tissue.[38,39] Because the densification level of WH was different from HAP, we successfully achieved a NC structure in WH ceramic by controlling the sintering temperature condition (900 °C) or the ratio of PEG (WH:PEG = 2:1 in wt %) (Figure S5).

In conjunction with the effort to understand the inner structure of the new ceramic composite, the capability of the NC-HAP to draw fluid was tested. As controls, nonporous HAP (NP-HAP) pellets and randomly porous HAP pellets, made using nonpressurized sintering processes were tested and each showed no fluid transport. In contrast, the NC-HAP drew fluid up very effectively from its reservoir at the base end of the pellet and delivered it to the upper surface located some 2 cm above the reservoir's fluid level. To visualize the

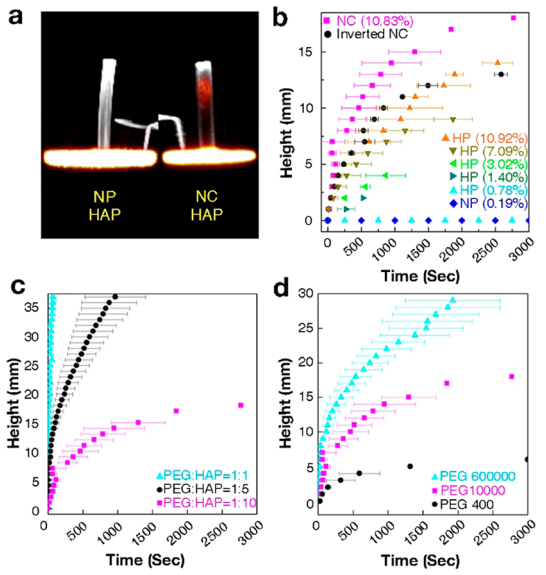

Figure 4. Fluid rise in hierarchically arborized nanochannels of a HAP ceramic material. (a) Fludeoxyglucose-positron emission tomography (FDG-PET) imaging showed that the nanochannel with gradually changing diameter formed in HAP ceramic (NC-HAP) sample (right) exhibited a greater fluid transport than a control nonporous HAP (NP-HAP) sample (left). (b) NC-HAP sample (magenta square), inverted orientation for NC-HAP sample (black circle), NP-HAP sample made from HAP/PEG at a ratio of 0.01% by weight (blue diamond) and homogeneously porous (HP) HAP samples (triangles) with various porosities were compared for their abilities to draw fluid in real time. The average porosity of each sample is indicated in brackets after their symbols. (c) Comparison of fluid rise height among HAP samples sintered with different ratios of PEG polymer. PEG:HAP = 1:10 (magenta square), PEG:HAP = 1:5 (black circle), PEG:HAP = 1:1 (cyan triangle). (d) Comparison of fluid rise height among HAP samples sintered with different molecular weights of PEG polymer. PEG MW 400 g mol^{-1} (black circle), PEG MW 10 000 g mol^{-1} (magenta square), PEG MW 600 000 g mol^{-1} (cyan triangle).

interior fluid transport *in situ* and to assess the difference in fluid migration between the NC-HAP and the NP-HAP pellets, ^{18}F-fluoro-deoxyglucose (FDG) positron emission tomography (PET) and computerized tomography (CT) scanning were performed (Figure 4a). Each pellet was placed vertically in a sterile container filled with distilled water containing ^{18}F-FDG and real-time images were acquired over a period of 60 min (Movie S3). In the NC-HAP pellet, ^{18}F-FDG migrated through the tapered nanochannels of the pellet. In contrast, there was no migration of ^{18}F-FDG in the conventional NP-HAP pellet indicating the absence of permeation or any diffusion. Consistent with the physical geometries of pore channels of varying diameters in the NC-HAP pellet, the CT image analysis showed a gradient of radiolucency along its length, overall being more radiolucent than the nonporous control pellet (Figure S6).

For further quantitative comparison, NC-HAP, NP-HAP, and randomly porous HAP samples were partially immersed in water in which a dye was dispersed to permit visualization of fluid movement. The rise of the dye-colored water within the samples were monitored and measured. The NC-HAP pellet, with its upwardly directed and narrowing channels, showed the fastest and the highest fluid rise (Figure 4b). When the NC-HAP pellet was placed in an inverted position with the channels widening toward the top, it also drew water but at a slower rate and to a lower height. There was no water rise in the NP-HAP (Φ = 0.19 $\pm$ 0.07%) or homogeneously porous HAP pellets of low porosity (Φ = 0.78 $\pm$ 0.08%) as the pores were isolated from each other. For a more direct comparison, we made homogeneously porous HAP pellets with the same porosity (Φ = 10.92 $\pm$ 2.00%) as the porosity of the NC-HAP pellets (Φ = 10.83 $\pm$ 1.65%), by altering the initial ratio of PEG and HAP in the composite mix. The fluid transport test showed that the final fluid rise was only slightly better for the NC-HAP than the homogeneously porous HAP pellet, but the rate of transport was clearly faster in the NC-HAP pellet, an outcome due to its tapered and hierarchical structure and high connectivity (see Figure 2 and Figure 3).

Further tests were conducted on samples engineered to have different porosities, created by incorporating different amounts of PEG of variable chain length. The results in Figure 4c showed that the samples containing larger amounts of PEG before sintering exhibited a higher and faster fluid rise due to an increase in the amount of both large and small channels, and thus a greater overall porosity. In addition, by varying the molecular weight of the PEG polymer from 400 to 600 000 g mol^{-1}, we were able to observe a correlation between the molecular weight of the polymer and the amount of fluid rise in the resulting NC-HAP pellet (Figure 4d). We attribute this correlation to the fact that PEG entangles more with itself and therefore agglomerates more when its molecular weight is larger.[30,32,33] However, agglomeration intensifies when samples are subjected to our pressurized sintering process; if the HAP-PEG mixture was sintered without pressure, the resulting pellets showed only small variation in porosity over a wide range of PEG molecular weight (Figure S7).

On the basis of these findings, we hypothesized that the NC-enabled HAP composite could mimic the supply of nutrients provided by the terminal supply network of natural hard tissues found in biological systems. In pursuit of this vision, we attempted to test whether NC-HAP blocks can indeed support the metabolism of living cells by efficiently supplying fluids and nutrients along the length of the material from a source restricted to the opposite end. To this propose, we tested the survival, growth and gene expression activity of human bone cells grown on the surface of the NC-HAP pellet, centimeters away from the media fluid reservoir. In these tests, an NC-HAP pellet was placed standing vertically up (nanochannels narrowing toward the top) in a sterile container filled with cell culture media, along with a control nonporous, but otherwise identical control HAP pellet, for comparison.

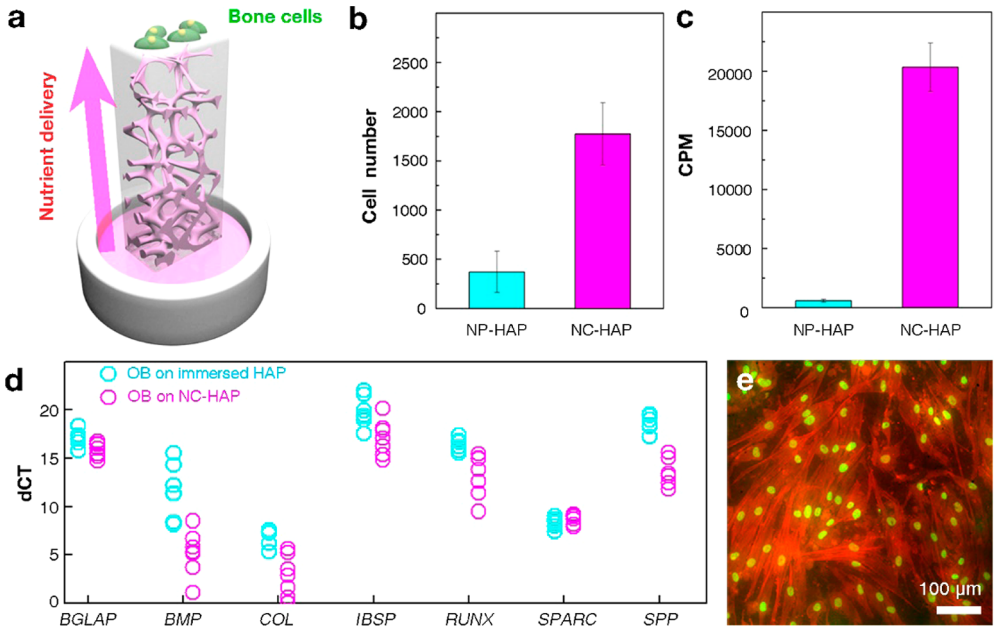

Figure 5. Human osteoblast cells grown on nanochannel with gradually changing diameter formed in HAP ceramic (NC-HAP) material. (a) Schematic representation of the method of seeding human osteoblasts onto the top surface of NC-HAP samples. (b) Cells grown on the top surface of NC-HAP, after 2 days of relying on the nutrient supply by nanochannels, showed a much greater number of cells (proliferation) than were grown on the top surface of NP-HAP samples. (c) Cellular uptake of ^{18}F-FDG on the top surface of NC-HAP was measured as orders of magnitude greater than the uptake and utilization of ^{18}F-FDG by cells grown on the NP-HAP samples. (d) Relative gene expression measured by quantitative real time PCR revealed that osteoblasts grown on top of NC-HAP samples (magenta, $n = 7$) expressed similar levels of bone-related genes compared to the expression profile for osteoblast cells grown on HAP material at the media to air interface as control (cyan, $n = 7$). (e) After 1 week, osteoblasts were observed growing on the surface of the NC-HAP samples, as shown by fluorescence microscopy.

Human-derived osteoblast cells (Lonza Clonetics) were seeded on the top surface of each pellet at a density of 1×10^5 cells ml^{-1}, where the surface area was approximately 7 mm $\times$ 2 mm. Containers were tightly sealed to prevent evaporative transport and maintained at 37 °C in an ambient atmosphere with 5% CO_2. The top surface of either of the HAP pellets upon which the osteoblast cells were seeded was approximately 1 cm above the nutrient media, as illustrated in Figure 5a. In this geometry, the osteoblast cells were maintained at the humidified air interface, with the only source of nutrients being drawn through the highly interconnected nanochannels of the NC-HAP ceramic over a distance of 1 cm. As the system inside the container maintained a vaporization-liquefaction process, fluid transport was able to continue by the evaporative loss at the surface of the HAP pellet, as well as by the cells incorporating the transported nutrients into macromolecules needed for cell proliferation and differentiation.

To directly confirm nutrient transport through NC-HAP, we detected cellular uptake of radioactive ^{18}F-fluoro-deoxyglucose (^{18}F-FDG) material by a gamma detector. After growing cells on top surface of NC-HAP in the air-exposed state for 24 h, we exchanged media to a low glucose formulation to restrict cells for glucose (Dulbecco's modified Eagle's medium with 1.0 g L^{-1} glucose, without L-glutamine:FBS:penicillin–streptomycin $\cong$ 90.1:9:0.9%), and after 24 h, added ^{18}F-FDG in aqueous solution to the bottom reservoir and collected the radio-labeled cells 1 h later. At this point, the number of cells was nearly 5 times greater for the NC-HAP pellet (1773 $\pm$ 316, $n = 3$) than that of NP-HAP pellet (370 $\pm$ 210, $n = 3$). In addition, from the gamma detection analysis, the uptake and incorporation of ^{18}F-FDG by these cells growing on the NC-HAP sample was orders of magnitude greater (20 330.1 $\pm$ 2053.7, $n = 3$) than that of the NP-HAP sample (594.9 $\pm$ 120.2, $n = 3$). These results indicate that transport of ^{18}F-FDG and cellular uptake was greatly enriched in the NC-HAP samples.

To ascertain that human bone cells grown on the nutrient-delivery surface of the NC-HAP pellet not only survive, but also maintained their differentiated phenotype for bone matrix production, the gene expression profiles for several bone-related proteins were assayed and compared to human osteoblast cells grown at the air to media interface atop the NP-HAP as the control. Messenger RNA (mRNA) levels for the two samples were identified using the standard technique of reverse transcription of mRNAs to complementary DNA strands followed by real time quantitative PCR analysis (RT-qPCR). Using this approach, the relative abundance of the mRNAs for each selected bone matrix gene was quantified as shown in Figure 5d. After 48 h of cell metabolism that depended solely on nutrient supply through the nanochannels of the NC-HAP, we found that the mRNAs for bone matrix-related

proteins were actively expressed and with expression levels comparable to those of control osteoblasts. The data from the RT-qPCR analysis indicated that the microenvironment created at the NC-HAP surface supported osteoblast cell gene expression in a manner equivalent to the standard technique of culturing bone cells at the media to air interface on a nonporous HAP surface.

After variable culture periods, the nuclei and actin cytoskeleton fibers were stained with DAPI and phalloidin, respectively, and the cells were observed using fluorescence microscopy. Notably, as shown in Figure 5e, the surface of the NC-HAP pellet showed vigorous osteoblast cell growth, whereas few osteoblast cells survived on the NP-HAP pellet. Cell proliferation is an increase in cell number and it is also an increase in the mass of new cells growing on the transport active surface of the NC-HAP pellet. The increased mass of the cells comes at the expense of the nutrients in the media that are transported through the NC-HAP to the cells. The cell proliferation, gene expression and ^{18}F-glucose incorporation into cells demonstrated through these corroborative approaches that nutrient supply through the hierarchically connected nanochannels was sufficient for these specialized osteoblast cells to proliferate and differentiate.

CONCLUSIONS

We developed a biologically inspired, hierarchically organized structure in ceramic to achieve effective directional fluid transport through a built-in network of capillary channels. A new pressure-gradient method was introduced and tested that created a long-range, highly interconnected nanochannel system in the ceramic biomaterial. This method is based on pressure-dependent polymer agglomeration and vaporization. The resulting system allows long-range, efficient transport of fluid and nutrients into sites and interfaces that conventional fluid conduction cannot reach without external force. Mammalian bone-forming cells placed at the distal transport termination of the nanochannel system were shown to proliferate in a manner dependent solely upon the supply of media by the self-powering nanochannels. It mimics the significant contribution that nanochannel transport plays in maintaining living hard tissues by providing nutrient supply that facilitates cell growth and healing, and thereby makes the ceramic composite "alive".

The findings in this work have the potential to impact in multiple areas where both mechanical strength and permeation are required, such as circulation in bioceramic implant, lubrication in ceramic motors, fuel transport and energy conversion.[40,41] Furthermore, it is known that living organisms metabolize most efficiently when resources are distributed throughout their tissues by a fractal network, resulting in minimal energy dissipation.[42] This work also introduced a novel and reproducible manufacturing technique for constructing such networked nanochannels within a ceramic biomaterial making use of pressure-gradient induced differentiations to polymer segregation between PEG and HAP.

METHODS

Preparation. Hydroxyapatite (HAP: $Ca_{10}(PO_4)_6(OH)_2$) was synthesized by a precipitation method with calcium hydroxide ($Ca(OH)_2$, 99.0%, High Purity Chemical, Japan) and phosphoric acid (H_3PO_4, 85.0%, Junsei Chemical Co., Ltd.) in an aqueous base. In distilled water, 0.5 M $Ca(OH)_2$ solution was prepared. After stirring vigorously with a mechanical stirrer (overhead stirrer, MSM-1 Jeio Tech) for an hour, 0.5 M H_3PO_4 was added drop-by-drop using a digital buret (Metrohm 876, Dosimat Plus). The final composition ratio of $Ca(OH)_2$ and H_3PO_4 was 10:6, and the precipitates were aged for 24 h while stirring at room temperature. The HAP solution was filter-pressed and freeze-dried. Dried HAP powder was mixed with polyethylene glycol (PEG: $HO{-}CH_2{-}(CH_2{-}O{-}CH_2{-})_n{-}CH_2{-}OH$) with molecular weights of MW 400 (M = 380−420 g mol^{-1}, Sigma-Aldrich), MW 2000 (M = 1800 g mol^{-1}, Merck), MW 10 000 (M = 9000 g mol^{-1}, Merck) and MW 600 000 (M = 600 000 g mol^{-1}, Sigma-Aldrich). Weight ratio of HAP and PEG was 10:1 in standard mixture. PEG was dissolved in distilled water and mixed until homogeneous with HAP by grinding.

Fabrication of Thin Layered PEG-HAP for Polymer Agglomeration Observation. PEG was dissolved in 1.5 mL g^{-1} of distilled water and mixed with HAP nanoparticles by grinding, in the selected weight ratios. The paste-like PEG-HAP mixture was deposited onto one slide and pinned between a second glass slide to form a thin layer. After 2 days of drying, samples were heated on a hot plate. The temperature was measured by a thermometer in contact with the surface of the hot plate. To apply pressure, the desired number of metal cubes (3.0 × 3.0 × 3.0 cm^3, 0.2 kg per metal cube) were stacked on the PEG-HAP sample. After 2 h of treatment to allow the PEG to agglomerate, the samples were removed from the hot plate and cooled to room temperature. To detect the PEG, we used reflected polarized light (Polarized Optical Microscopy, Olympus BX51) as the crystallized PEG was birefringent.

Fabrication of NC-HAP Pellet. To make NC-HAP pellets of selected defined porosity, various ratios of HAP-PEG mixture (PEG:HAP = 1:1, 1:5, 1:10) were made into pellets in a 37 mm × 7 mm × 2 mm aspect shape, using a pressure mold, by applying 2 tons of pressure for 3 s. The HAP-PEG pellets were sintered at 1100 °C for 2 h. During sintering of the NC-HAP pellet, a 911.1 g mass right-triangular prism-shaped metal wedge, made from stainless steel (SUS310S) or super alloy (HAYNES230), was placed atop the HAP-PEG pellet to provide a pressure gradient that reflected the shape and mass of the wedge. An alumina ceramic (Al_2O_3) plate was placed between the metal weight and the HAP-PEG pellet to prevent contamination.

Fabrication of Nonporous HAP Pellet and Homogeneously Porous HAP Pellet. To make nonporous HAP (NP-HAP) pellets, the PEG binder at 0.0001% by weight, was mixed with HAP powder. To regulate the porosity of the homogeneously porous HAP pellet, the initial ratio between PEG and HAP was controlled by mixing HAP and PEG at a ratio of: 2.55:1, 2.63:1, 3.25:1, 4.95:1 and 10:1. The HAP-PEG mixtures were made into pellets in a 37 mm × 7 mm × 2 mm aspect shape, using a pressure mold, by applying 2 tons of pressure for 3 s and sintered at 1100 and 1300 °C for 2 h to make homogeneously porous HAP pellet and NP-HAP pellet, respectively. The porosities of NP-HAP pellets and homogeneously porous HAP pellets (HAP:PEG = 2.55:1, 2.63:1, 3.25:1,

4.95:1 and 10:1) were 0.19 ± 0.07% (n = 4), 10.92 ± 2.00% (n = 6), 7.09 ± 0.27% (n = 4), 3.02 ± 0.29% (n = 4), 1.40 ± 0.16% (n = 4) and 0.78 ± 0.08% (n = 5), respectively.

Characterization and Analysis. The surface morphology of the NC-HAP was observed by field emission scanning electron microscope (JSM-6330F, JEOL).

The images of stained osteoblast cells were obtained using fluorescence microscopy (Axio Observer Inverted Microscope, Carl Zeiss).

Porosity Analysis. The NC-HAP sample was divided into three regions corresponding to variation in the pressure gradient (pressure region 0−4, 4−8 and 8−12, See Figure 2a) to provide the corresponding regions of varied porosity. Gas adsorption−desorption was measured in each of the three regions. N_2 adsorption was measured at 77 K on a BELSORP-mini II (BEL Japan Inc., Japan) after degassing under vacuum at 150 °C for 24 h. Specific surface area was estimated using the BET (Brunauer−Emmett−Teller) equation with a 0.01−0.20 relative pressure range. The porosity of each region of NC-HAP was calculated by Archimedes' principle, represented as ((immersed mass-dried mass) × (immersed mass-suspended mass)$^{-1}$ × 100%) by using an electronic scale (GR-200, AND) equipped to measure specific gravity (AD-1653, AND).

The distributions of low-density pixels in each region of the NC-HAP sample were analyzed by Micro-CT (ZEISS Xradia 510 Versa), according to the porosity measured by Archimedes' principle. The connectivity among the low-density pixels in each region was analyzed using the Amira software.

Mechanical Test. In order to evaluate the mechanical properties of the pressure-induced varied porosity regions of the NC-HAP, micro-Vickers hardness was measured. Maximum load and dwell time were 4.9 N and 5 s, respectively. Ten points on each cross-section were tested.

FIB-FESEM 3D Reconstruction and HRTEM Analysis. To reconstruct 3D images and movies of interconnected pore structures, FIB-FESEM tomography was used (Auriga, Carl Zeiss). Different region from an NC-HAP sample that correspond to different measurements of the pressure gradient (sections with pressure level 6−9 and pressure level 3−6, see Figure 2a) were sectioned by FIB, and digitally imaged with a magnification of ×32 000. The total number of slices analyzed was 200 and the interval between each slice was 15 nm. Milling current was 120 pA and the tilting angle was approximately 54°. The 3D image processing program Amira (Carl Zeiss, version 5.3.3) was used to define regions of interest (ROI) and to construct 3D images with dimensions 4.0 × 3.7 × 3.0 μm^3. A focused ion beam (FESEM-FIB, FEI NOVA Nanolab 200 dual beam system) was used to take samples. A platinum gas injection system was applied to adhere grids and to form deposit for protecting the microstructure of the samples. A high-energy Ga ion beam (30 kV, 7 nA ∼ 20 nA) was used to analyze the microstructure of the pellets. A low-energy Ga ion beam was used for cross-sectioning (30 kV, 50 pA ∼ 5 nA) and cleaning (5 kV, 70 pA) during the TEM sampling and Nano-CT sampling process.

Higher emission was needed to make larger cylindrical samples for 3D reconstruction using synchrotron radiation (PLS, Pohang Light Source). Samples were removed using an Omniprobe system (Tungsten needle, Omniprobe) with a sharp tip. TEM samples were attached to a 3-post Cu grid (Ted Pella, Inc.), Nano-CT samples were loaded with the aid of a needle (Korea Vaccine CO., LTD) and the samples were placed on a copper mesh grid (Ted Pella, Inc.). Nanosize pores of HAP were measured by high-resolution transmission electron microscopy (FEI, Tecnai F20) study and energy dispersive spectrometry (EDAX) techniques.

Cyclotron 7C XNI Imaging. Experiments were carried out using the 7C (XNI) beamline of the Pohang Light Source. High flux monochromatic 6.7 keV X-rays were focused using beryllium compound refractive lenses (f = 3.5 m). The sample was positioned at the focal point of the lenses. The beam size at the sample position was around 50 μm and the estimated photon flux was 10^{12} photons sec^{-1}. In order to reduce spatial coherency and homogenize the illumination, a diffuser was installed in front of the sample. The sample was mounted on a three-axis piezo-driven scanning stage on top of an air-bearing rotation stage. A 140 μm diameter tungsten zone plate with an outermost zone of width 50 nm and 1 μm thickness was used to magnify the X-ray image to achieve 40 nm resolution. For phase contrast, a holed (5 μm diameter) aluminum-film phase plate of 3.87 μm ± < 1% thickness was positioned in the back focal plane of the zone plate. The thickness was selected so as to phase shift the diffracted beam by 0.5π and thereby make the sample image darker in the bright field. The detector, consisting of a thin (10 μm) Tb:LSO scintillator crystal and an ×20 optical microscope, was placed 2.46 m downstream of the sample. The CCD of the optical microscope was 2048 × 2048 pixels of 18 μm size. The total magnification of the system was ×1230 and the corresponding effective pixel size was 15 nm. 3D tomographic images were made from 181 images that were collected over an angular range of 180° each with 10 s of exposure time.

^{18}F-Fluoro-Deoxyglucose Positron Emission Tomography (FDG-PET). To compare fluid migration *in situ* for NC-HAP and NP-HAP pellets, ^{18}F-fluoro-deoxyglucose (FDG) positron emission tomographic (PET) and computed tomography (CT) scanning were performed (NanoPET/CT, Mediso, Medical Imaging Systems, Budapest, Hungary). Each pellet was oriented vertically in a sterile container filled with 3 mL of distilled water containing ^{18}F-FDG (100 *u*Ci). The PET image was acquired by scanning in list mode for 60 min and the images were reconstructed. CT and PET images were acquired and reconstructed as maximal intensity projection images. Images were compared using the same image window settings for all images.

Fluid Rise Test. The fluid rise test was performed in a double walled vessel to control temperature. Cooled isopropanol was circulated between the double walls of the vessel to maintain the inside container at a constant temperature of 25 °C. To fix the humidity level at a constant value, the bottom of the inside container was covered with silica gel blue (DaeJung) and Drierite (Hammond Company). NC-HAP, NP-HAP, and homogeneously porous HAP pellets were partially immersed vertically in distilled water. A 1 mm calibrated scale was used to measure the rise of fluid using a red ink dye. The number of samples used for each conditions was n = 3.

Cell Culture and Staining. To observe the growth of human osteoblasts on HAP surfaces exposed to air, blocks of HAP were prepared as described. NC-HAP pellets were compared with NP-HAP pellets as controls. After sintering, the HAP pellets were washed with acetone and distilled water, sterilized at 130 °C for 20 min and dried under UV irradiation. A sterilized pellet was placed upright in a plastic tube, forming a reservoir for the osteoblast basal medium (Lonza Clonetics) containing fetal bovine serum (FBS), ascorbic acid and GA-1000. Human osteoblasts (Lonza Clonetics) were seeded on the top surface, which measured 7 mm × 2 mm, at a density of 1 × 10^5 cells ml^{-1}. The sample was placed in a water-jacketed incubator maintained at 37 °C in ambient atmosphere supplemented with 5% CO_2. After cell attachment, the medium was partially removed to a level approximately 1 cm below the top surface of the HAP pellet. After 7 days of culture, the pellet was fixed for 10 min with 3.7% formaldehyde diluted in PBS (Cellgro, Mediatech Inc.). The cells were permeabilized with 0.2% Triton X-100 diluted in PBS for 10 min. The actin cytoskeleton network was stained with phalloidin (Phalloidin, fluorescein isothiocyanate labeled, Sigma) for 1 h and nuclei were stained with DAPI (4′,6-diamidino-2-phenylindole dihydrochloride, Sigma) for 5 min. The NC-HAP pellet was mounted with Fluoromount (Aqueous Mounting Medium, Sigma) and observed by fluorescence microscopy with appropriate excitation and barrier filters.

Cell Proliferation and Cellular Uptake of ^{18}F-FDG. Cells were maintained on the top surface of NC-HAP as described for 1 day with the media exchanged for a low glucose formulation (Dulbecco's modified Eagle's medium with 1.0 g L^{-1} glucose, without L-glutamine, FBS, 10% v v^{-1}, penicillin 10 000 units mL^{-1}, streptomycin 10 mg mL^{-1}) to starve cells for glucose. Likewise, low-glucose media was carefully provided to the reservoir to a level approximately 1 cm below the surface of the NC-HAP on which the cells grew. After 1 day, low-glucose media was changed with ^{18}F-FDG (0.5 *u*Ci sample^{-1}) in PBS, to the same height level. After 1 h, the NC-HAP sample was recovered and its surfaces, except the top surface supporting the cells,

were carefully wiped with tissue paper. The NC-HAP sample, except the surface supporting the osteoblasts, was washed several times with phosphate buffered saline (PBS) to remove ^{18}F-FDG not incorporated into the osteoblast cells. Cells were released from the NC-HAP sample using 3 mL of trypsin-EDTA solution for 3 min and the cells recovered. The trypsin-EDTA was neutralized with 7 mL of media and the cells were collected by brief centrifugation at 3000 rpm for 3 min and the wash solution discarded. Using a cell counter (ADAM-MC, nanoEntek) and a gamma detector (Wallac 1480 Wizard 3 gamma counter, Turku, Finland), the total cell number was quantified and the radioactive counts per minute (CPM) incorporated into the cells was measured, respectively. For the control sample, exactly the same experimental protocol was conducted only with a NP-HAP samples with cell number and radioactive incorporation determined compared with that from the NC-HAP.

Real Time PCR. Real time PCR was performed with Rotor gene Q (Qiagen, Santa Clarita, CA) with the Rotor gene SYBR green PCR kit. RNA was extracted from cells using a RNA extraction reagent (RNAiso Plus, Takara), and first strand cDNA was synthesized by using a QuantiTect reverse transcription kit (Qiagen) with random hexamer primers. The initial activation step for PCR was 3 min at 95 °C. Denaturation and combined annealing/extension cycles proceeded at 95 °C for 3 s and 60 °C for 10 s, respectively. Each sample was subjected to analysis in triplicate. The numbers of samples used for NC-HAP and for the control nonporous HAP were both $n = 7$. The relative quantities of amplified cDNAs were calculated using the ΔC_T method with rRNA used as the baseline. Primers used for PCR were purchased from QuantiTect Primer Assay (Qiagen): 18S rRNA (*RRN18S*, QT00199367), secreted protein acidic cysteine-rich (*SPARC*, QT00018620), bone gamma-carboxyglutamate (Gla) protein (*BGLAP*, QT00232771), bone morphogenetic protein 2 (*BMP2*, QT00012544), secreted phosphoprotein 1 (*SPP1*, QT01008798), collagen type I (*COL1*, QT00037793), Runt-related transcription factor 2 (*RUNX2*, QT00020517), and integrin-binding sialoprotein (*BSP*, QT00093709).

Conflict of Interest: The authors declare no competing financial interest.

Acknowledgment. This research was supported by the Basic Science Research Program, through the National Research Foundation of Korea (NRF), funded by the Ministry of Science, ICT & Future (No. Grant Number: 2011-0011225); the Global Frontier R&D Program on Center for Multiscale Energy System funded by the National Research Foundation under the Ministry of Science, ICT & Future, Korea (0420-20130104); the International Research & Development Program of the National Research Foundation of Korea (NRF), funded by the Ministry of Science, ICT & Future Planning (No. 2013K1A3A1A32035536); and at Brown University by an Air Force Office of Scientific Research (AFOSR) grant for functional composite materials and seed funding from Brown's Institute of Brain Sciences. MLS was supported by National Institute for Dental and Craniofacial Research Grant R37 DE13045 from the National Institutes of Health, U.S. Public Health Service. KL and HNH were supported by the Basic Science Research Program through the National Research Foundation in Korea funded by the Ministry of Science, ICT, and Future Planning (NRF-2013R1A2A2A01008806).

Supporting Information Available: Detailed calculation of pressure loading gradient on NC-HAP, polymer agglomeration mechanism in PEG-HAP composite during the pressurized sintering process, FESEM and TEM EELS analyses of nanopores, micro CT scanning of NC-HAP pellet, nanochannel reconstruction from FIB-FESEM tomography and synchrotron X-ray nano-imaging, and ^{18}F-fluoro-deoxyglucose (FDG) positron emission tomographic (PET) video of ascending liquid in NC-HAP pellet is provided. This material is available free of charge *via* the Internet at http://pubs.acs.org.

REFERENCES AND NOTES

1. Bejan, A.; Lorente, S. Constructal Theory of Generation of Configuration in Nature and Engineering. *J. Appl. Phys.* **2006**, *100*, 041301.
2. Zheng, Y. M.; Bai, H.; Huang, Z. B.; Tian, X. L.; Nie, F. Q.; Zhao, Y.; Zhai, J.; Jiang, L. Directional Water Collection on Wetted Spider Silk. *Nature* **2010**, *463*, 640–643.
3. Prakash, M.; Quere, D.; Bush, J. W. M. Surface Tension Transport of Prey by Feeding Shorebirds: The Capillary Ratchet. *Science* **2008**, *320*, 931–934.
4. Parker, A. R.; Lawrence, C. R. Water Capture by a Desert Beetle. *Nature* **2001**, *414*, 33–34.
5. Brookes, M.; Elkin, A. C.; Harrison, R. G.; Heald, C. B. A New Concept of Capillary Circulation in Bone Cortex: Some Clinical Applications. *Lancet* **1961**, *277*, 1078–1081.
6. Dickson, K. M.; Bergeron, J. J. M.; Philip, A.; O'Connor-McCourt, M.; Warshawsky, H. Localization of Specific Binding Sites for I-125-Tgf-Beta 1 to Fenestrated Endothelium in Bone and Anastomosing Capillary Networks in Enamel Organ Suggests a Role for Tgf-Beta 1 in Angiogenesis. *Calcif. Tissue Int.* **2001**, *68*, 304–315.
7. Zhou, J.; Wang, S. T.; Nie, F. Q.; Feng, L.; Zhu, G. S.; Jiang, L. Elaborate Architecture of the Hierarchical Hen's Eggshell. *Nano Res.* **2011**, *4*, 171–179.
8. Seidl, B.; Huemer, K.; Neues, F.; Hild, S.; Epple, M.; Ziegler, A. Ultrastructure and Mineral Distribution in the Tergite Cuticle of the Beach Isopod *Tylos europaeus* Arcangeli, 1938. *J. Struct. Biol.* **2011**, *174*, 512–526.
9. Nogueiras-Nieto, L.; Gomez-Amoza, J. L.; Delgado-Charro, M. B.; Otero-Espinar, F. J. Hydration and *N*-Acetyl-L-Cysteine Alter the Microstructure of Human Nail and Bovine Hoof: Implications for Drug Delivery. *J. Controlled Release* **2011**, *156*, 337–344.
10. Hollister, S. J. Porous Scaffold Design for Tissue Engineering. *Nat. Mater.* **2005**, *4*, 518–524.
11. Deville, S. Freeze-Casting of Porous Ceramics: A Review of Current Achievements and Issues. *Adv. Eng. Mater.* **2008**, *10*, 155–169.
12. Barber, R. W.; Emerson, D. R. Optimal Design of Microfluidic Networks Using Biologically Inspired Principles. *Microfluid. Nanofluid.* **2008**, *4*, 179–191.
13. Eijkel, J. Scaling Revisited. *Lab Chip* **2007**, *7*, 1630–1632.
14. Shou, D.; Ye, L.; Fan, J.; Fu, K. Optimal Design of Porous Structures for the Fastest Liquid Absorption. *Langmuir* **2013**, *30*, 149–155.
15. Bal, K.; Fan, J.; Sarkar, M.; Ye, L. Differential Spontaneous Capillary Flow through Heterogeneous Porous Media. *Int. J. Heat Mass Transfer* **2011**, *54*, 3096–3099.
16. Fan, J.; Sarkar, M.; Szeto, Y.; Tao, X. Plant Structured Textile Fabrics. *Mater. Lett.* **2007**, *61*, 561–565.
17. Shou, D.; Ye, L.; Fan, J.; Fu, K.; Mei, M.; Wang, H.; Chen, Q. Geometry-Induced Asymmetric Capillary Flow. *Langmuir* **2014**, *30*, 5448–5454.
18. Reyssat, M.; Sangne, L.; van Nierop, E.; Stone, H. Imbibition in Layered Systems of Packed Beads. *Europhys. Lett.* **2009**, *86*, 56002.
19. Renvoisé, P.; Bush, J.; Prakash, M.; Quéré, D. Drop Propulsion in Tapered Tubes. *Europhys. Lett.* **2009**, *86*, 64003.
20. Rubega, M. A.; Obst, B. S. Surface-Tension Feeding in Phalaropes: Discovery of a Novel Feeding Mechanism. *Auk* **1993**, *110*, 169–178.
21. Chung, S.; Yun, H.; Kamm, R. D. Nanointerstice-Driven Microflow. *Small* **2009**, *5*, 609–613.
22. Ronca, G.; Russell, T. P. Thermodynamics of Phase Separation in Polymer Mixtures. *Macromolecules* **1985**, *18*, 665–670.
23. Feldman, K. E.; Kade, M. J.; Meijer, E.; Hawker, C. J.; Kramer, E. J. Phase Behavior of Complementary Multiply Hydrogen Bonded End-Functional Polymer Blends. *Macromolecules* **2010**, *43*, 5121–5127.
24. Singh, R.; Tolouei, R.; Tan, C. Y.; Aw, K.; Yeo, W. H.; Sopyan, I.; Teng, W. D. Sintering of Hydroxyapatite Ceramic Produced by Wet Chemical Method. *Adv. Mater. Res.* **2011**, *264*, 1856–1861.
25. Ramesh, S.; Tan, C. Y.; Tolouei, R.; Amiriyan, M.; Purbolaksono, J.; Sopyan, I.; Teng, W. D. Sintering Behavior of Hydroxyapatite Prepared from Different Routes. *Mater. Des.* **2012**, *34*, 148–154.

26. Cho, J. S.; Rhee, S.-H. Formation Mechanism of Nano-Sized Hydroxyapatite Powders through Spray Pyrolysis of a Calcium Phosphate Solution Containing Polyethylene Glycol. *J. Eur. Ceram. Soc.* **2013**, *33*, 233–241.
27. Balazs, A. C.; Emrick, T.; Russell, T. P. Nanoparticle Polymer Composites: Where Two Small Worlds Meet. *Science* **2006**, *314*, 1107–1110.
28. Gupta, S.; Zhang, Q.; Emrick, T.; Balazs, A. C.; Russell, T. P. Entropy-Driven Segregation of Nanoparticles to Cracks in Multilayered Composite Polymer Structures. *Nat. Mater.* **2006**, *5*, 229–233.
29. Gupta, S.; Zhang, Q.; Emrick, T.; Russell, T. P. "Self-Corralling" Nanorods under an Applied Electric Field. *Nano Lett.* **2006**, *6*, 2066–2069.
30. Sakellariou, P.; Rowe, R. C.; White, E. F. T. An Evaluation of the Interaction and Plasticizing Efficiency of the Polyethylene Glycols in Ethyl Cellulose and Hydroxypropyl Methylcellulose Films Using the Torsional Braid Pendulum. *Int. J. Pharm.* **1986**, *31*, 55–64.
31. Ozdemir, C.; Guner, A. Solution Thermodynamics of Poly(Ethylene Glycol)/Water Systems. *J. Appl. Polym. Sci.* **2006**, *101*, 203–216.
32. McNamee, C. E.; Yamamoto, S.; Higashitani, K. Effect of the Physicochemical Properties of Poly(Ethylene Glycol) Brushes on Their Binding to Cells. *Biophys. J.* **2007**, *93*, 324–334.
33. Trimm, D. L.; Stanislaus, A. The Control of Pore-Size in Alumina Catalyst Supports—a Review. *Appl. Catal.* **1986**, *21*, 215–238.
34. Chaklader, A. C. D. 'Reactive Hot Pressing': a New Ceramic Process. *Nature* **1965**, *206*, 392–393.
35. Yang, J. F.; Zhang, G. J.; Ohji, T. Porosity and Microstructure Control of Porous Ceramics by Partial Hot Pressing. *J. Mater. Res.* **2001**, *16*, 1916–1918.
36. Weibel, A.; Bouchet, R.; Denoyel, R.; Knauth, P. Hot Pressing of Nanocrystalline TiO_2 (Anatase) Ceramics with Controlled Microstructure. *J. Eur. Ceram. Soc.* **2007**, *27*, 2641–2646.
37. Ding, M.; Odgaard, A.; Hvid, I. Accuracy of Cancellous Bone Volume Fraction Measured by Micro-CT Scanning. *J. Biomech.* **1999**, *32*, 323–326.
38. Driessens, F. C. M.; Verbeeck, R. M. H. *Biominerals*; CRC Press: Boca Raton, FL, 1990.
39. Jang, H. L.; Jin, K.; Lee, J.; Kim, Y.; Nahm, S. H.; Hong, K. S.; Nam, K. T. Revisiting Whitlockite, the Second Most Abundant Biomineral in Bone: Nanocrystal Synthesis in Physiologically Relevant Conditions and Biocompatibility Evaluation. *ACS Nano* **2013**, *8*, 634–641.
40. Sparreboom, W.; van den Berg, A.; Eijkel, J. C. T. Principles and Applications of Nanofluidic Transport. *Nat. Nanotechnol.* **2009**, *4*, 713–720.
41. Sparreboom, W.; van den Berg, A.; Eijkel, J. C. T. Transport in Nanofluidic Systems: A Review of Theory and Applications. *New J. Phys.* **2010**, *12*, 015004.
42. Banavar, J. R.; Maritan, A.; Rinaldo, A. Size and Form in Efficient Transportation Networks. *Nature* **1999**, *399*, 130–132.